Turkish Online Journal of Qualitative Inquiry (TOJQI)
Volume 12, Issue 5, July 2021: 4604-4634

Research Article

Optimal Fuel Consumption Using FUZZY-PI Based RSC Control Strategy on Wind Driven DFIG, DG and Solar PV Array

P. Siva Krishna [1], M. Anitha [2], P. Venkata Mahesh [3], N. Dharani Kumar [4],
Ch. Ranga Rao [5], Dr. N.C. Kotaiah [6]

Abstract

This article focuses on creating a new method to dynamically optimize DFIG controllers in all wind speed situations using a WT-driven DFIG. Fuzzy-PI is recommended to optimize the damping ratios of the system eigenvalues in small signal control design by optimizing settings of PI controllers of DFIG's rotor side (RSC) at various wind speeds. System control systems such as FLC are lately used in order to adjust system behavior and operations to match predefined specifications. For grid or load linked linear or non-linear loads, the FLC system may enhance the tracking performance as compared to conventional control systems. Fuzzy Predictive Control (FPC) is a hybrid control system that incorporates an FLC system controller with an MPC in order to achieve rapid responsiveness of the output signal. The FLC has been developed and trained on the wind data set to provide optimum values and have the capacity to accurately predict such values in a short time frame. Flexible PI controller systems (such as FLC) are intended to adjust PI gain values when the wind speed changes. Using MATLAB software for a grid DFIG system, and a DG system, simulation was carried out. A transitory improvement across a broad wind speed range may be achieved using FLC based DFIG adaptive PI control.

Keywords: *Wind turbine, Doubly fed induction generator(DFIG), Diesel generator, Solar photovoltaic array, Bidirectional buck/boost DC-DC converter, battery energy storage, Power quality.*

[1] Asst.Professor, R.V.R & J.C College of Engineering (psivakrishanan@gmail.com)

[2] Asst.Professor, R.V.R & J.C College of Engineering (mallipeddianitha@gmail.com)

[3] Asst.Professor, R.V.R & J.C College of Engineering (vnktmahesh@gmail.com)

[4] Asst.Professor, R.V.R & J.C College of Engineering (dharaninarne@gmail.com)

[5] Asst.Professor, R.V.R & J.C College of Engineering (chegudi.rangarao@gmail.com)

[6] Professor, R.V.R & J.C College of Engineering (nckotaiah@rvrjc.ac.in)

I. INTRODUCTION

The benefits of DGs to residents of urban dwelling is what attracts people to use diesel generators (DGs) as backup power for the following reasons [1] to [3]. It is essential that conversion efficiency be much greater than other energy sources to keep total greenhouse gas emissions low. They are often seen in facilities dispersal of islands, military and commercial ships, and everything else, for these reasons. Unfortunately, noise and air pollution are often problems associated with DGs. The operating cost relies on the amount of fuel used by the plant, in conjunction with its power output. In this case, using renewable energy (RE) like wind, solar, and biomass results in a cost reduction. In addition, RE energy sources, which are highly dependent on the environment, are free of pollution and abundant. More so than from the list of sources, it is expected that wind and solar would be more widely accepted because of their cheaper cost and recent technical advances. 5;6 On the whole, wind turbines are considered fixed velocity and variable speed machines. More so than for any other kind of wind turbine, wind turbines with simple in operation characteristics have a market advantage. On the other hand, they also experience extra power loss. For the most majority of wind turbine installations, variable speed wind turbines with a doubly fed induction generator (DFIG) are utilized, because they have the following advantages: decreased device rating, less acoustic noise, highly cheap energy usage, and minimal power loss. The vast majority of DFIG-based wind energy systems literature is all focused on standalone and grid linked systems [8] [9] through [11]. The authors have provided DFIG based WECS that is operated independently from an external power source as well as using electric battery energy storage (BES) that is linked directly to the DC connection. BES is also discussed while comparing performance before and after the use of BES. For [9], the authors show how a successful functioning of turbine linked DFIG may be obtained by using an associate degree extended active power theory that has both unbalanced and balanced grid circumstances. Lastly, the DFIG is being managed via just rotor facet device management (RSC). Facility issues specifically affect how well the architecture handles harmonic loads. Liu et al. [10] have studied the correlation between the DFIG wind energy facility characteristics and grid strength when it is linked to the grid. A validation experiment has, however, not been done. In [11], the authors have covered a technique for grid-synchronization control for smooth DFIG association. Additionally, the IEEE thirty-nine bus system has had this requirement enforced on a newly implemented real-time simulation platform. To yet, however, hardware implementation has not been completed. Solar photovoltaic (PV) array power production has

seen a growing trend on the alternative side. Single-stage and double-stage solar energy conversion systems are also possible. A considerable amount of material that deals with solar power systems is included in the papers in [12], [13]. There is no denying that Iran's Shah and others [12] have incontestable evidence for the one-stage SECS linked to the electrical grid. Moreover, voltage source conversion using a simple current extraction method has been implemented using a second-order generalized planimeter supported by a frequency-locked loop (VSC). In [13], the authors have conferred the SECS to the grid. Additional steps have also been taken to address the facility quality problems by implementing an associate degree adjustive algorithmic rule of fast zero attracting normalized least mean fourth. It isn't cheap and dependable due to their intermittent functioning. Because of this, combining each source of wind and sun energy, increases the power supply's dependability Fourteen, fifteen. The study conducted by Morshed et al. [14] reveals a wind-PV system that has fault ride-through capabilities. While in its architecture, the solar PV array is linked to the DFIG DC link with WECS via a power converter and a DC-DC converter, the solar PV array has a unique DC connection. However, more DC-DC converters and grid-side converters will generate more DC power losses and expense. With regard to [15], the authors have said that the wind-solar PV system with BES in standalone mode has been proven without a doubt. The solar PV array is linked to the DC link of the wind turbine via a boost converter in its current setup. However, since it is directly linked at the DC connection, the presence at the BES is not under control. Additionally, microgrids enabled distributed generation (DG), wind and solar power resources were created and were both reported in the literature [16]-[18]." The capability described in [16] has come up with for a microgrid whose components include wind, solar, and diesel power sources distributed across an island. However, no discussion of the best fuel combination for DG has been presented." The authors in [17] are certain of an integrated wind-diesel microgrid capable of generating clean energy in fuel-efficient zones with BES. The current coming from the BES is regulated directly via the DC connection. Also, just 1 RE supply is required for getting aloof from fuel-economy zone. Wind, solar, and diesel microgrids with BES are created for sure distant areas by Venkatraman et al. [18]. While developing the source and cargo controllers, the optimal performance of the metric weight unit has been overlooked. The BES has a crucial function in pairing generation and demand in any microgrid. Additionally, it contributes to the extraction of most electricity from wind and solar production, which happens when generation exceeds demand. Various MPPT (maximum power point tracking) methods are mentioned in the literature, for wind and solar energy; each is tailored to get the greatest amount of power at certain wind speeds

and insolation, which vary across studies. This study offers a DFIG (dg and solar PV) array with BES (Beyond Energy System) in order to decrease the fuel consumption of DFIGs. A social unit's need for bottom-load distribution, specified by a particular location, is delivered by the DG. Among the findings of this research, some of the most important have to do with managerial strategies. In order to keep the Dg operational in the most fuel-efficient operating mode, a totally new, generalized concept is used. The load side device control (LSC) is intended to control dg harmonics compensation and reactive power compensation along with power quality issues. Most of the wind turbine's electricity is extracted by the RSC.

II. CONFIGARATION OF MICROGRID

BES is linked to the common DC bus of back-back connected VSCs via a buck/boost DC-DC converter with two faceplates. This company intends to provide a route for the mechanical device power that exceeds DFIG's needs. Additionally, a solar PV array is linked to the DC bus directly. The bidirectional DC-DC converter buck/boost control is intended to maximize the solar array power and regulate the output of the current. The algorithm has been altered to obtain the most power from the solar panel. By imposing a minimal variety of converters, this microgrid design reduces the sector of the economy and switching losses. The IEEE 519 standard is adhered to in regards to the DFIG stator voltage and dg currents. This wind-diesel-solar microgrid, utilizing BES, is modeled and simulated in the MATLAB Sim Power Systems Toolbox using the Sim Power Systems utility tool. Varying sustained winds, variable insolation, effect on buck boost device, and buck boost device, impacted by mass, are all included into system performance (PCC). To verify the microgrid functionality, a prototype is built in the laboratory and then tested in the field.

The microgrid's schematic configuration is shown in Fig. 1. This kind of energy generation includes wind turbines, DFIG, DG, solar PV arrays, BES, bidirectional buck/boost DC-DC converters, RSC, LSC, inductors, Δ/Y transformers, linear and nonlinear loads, circuit breakers (CB1 & CB2), DC link capacitor, and ripple filters. This microgrid is tailored to serve the demands of a specific locale with a peak capacity of 7.5 kW. They have been built to produce 7.5 kW of electricity each, which is a total of 12.5 kW. The following power distribution method includes a solar PV array that is linked to DC link without going via a bidirectional buck/boost DC-DC converter. a 4-pole internal combustion engine that generates 4 stroke, reciprocal movements with automated voltage regulator (voltage regulator is included in the machine) (AVR). In terms of rated capacity, a 7.5 kW DG is chosen. DG, BES, and other components have the design process carried out in the literature references

[12], [15], [17]. In addition, the design parameters of microgrid, which are included in Appendices, are considered.

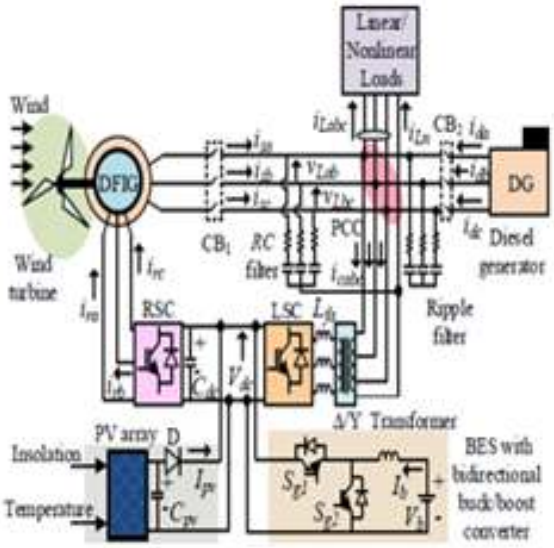

Figure 1. DFIG based microgrid

A.Control Algorithm for RSC

In Fig. 2, the RSC control method is shown. RSC is often used to fulfill the DFIG's power reactive requirement for RSC.

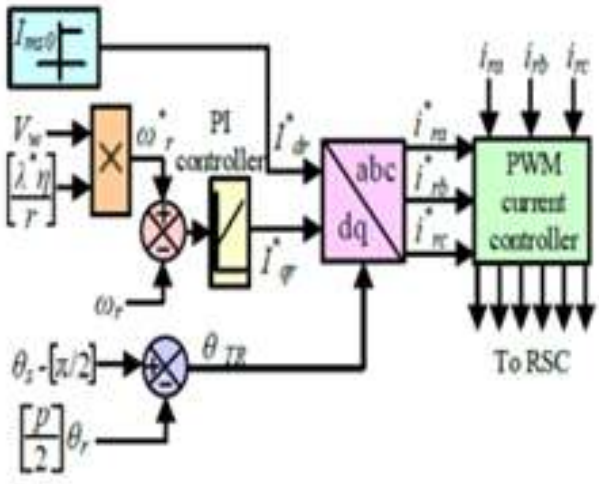

Figure 2. RSC control algorithm

Additionally, to control the speed of the wind turbine for meeting the MPPT goal. The FOVC technique, illustrated in Fig. 2, is used to RSC to produce the switching pulses. In FOVC, I*dr and I*qr indicate reactive and active rotor currents, respectively. It may be calculated as [21] that the I*dr is equivalent to no loading magnetizing current (Ims0) for DFIG.

$$I_{mr0} = \frac{\sqrt{2}V_L}{\sqrt{3}X_m} \quad (1)$$

VL is the process hazard at the machine terminals, and Xm is the magnetic flux reactance of the machine.

It is calculated as shown in Fig. 2 and therefore is obtained as,

$$I'_{qr(k)} = I'_{qr(k-1)} + K_{p\omega}\left(\omega_{err(k)} - \omega_{err(k-1)}\right) + K_{i\omega}\omega_{err(k)} \quad (2)$$

For PI speed controller proportional and integral constants, Kpω and Kiω may be used. Speed error is represented by the ωerr(k) and ωerr(k-1) symbols.

In the case of ωerr(k), it is calculated as,

$$\omega_{err(k)} = \omega^*_{r(k)} - \omega_{r(k)} \quad (3)$$

At kth instance, DFIG's reference and detected rotor speeds are denoted as ω*r(k) and ωr(k).

Tip - speed MPPT control [19] provides the reference rotor speed.

$$\omega_r^* = \eta\lambda^* V_w / r \quad (4)$$

It may be said that the following formulas, where Vwλ*,η, and r indicate wind speed, optimum tip speed ratio, gear ratio, and diameter of wind turbine, respectively, can be derived.

θTR is calculated as:

$$\theta_{TR} = \left(\theta_r - \frac{\pi}{2}\right) - \left(p/2\right)\theta_r \quad (5)$$

where the phase locked loop yields θs, and where the measured rotor speed yields,

$$I'_{dr} - \left(\sqrt{2/3}\right) \times \left(\frac{P_0^* \times VA_{DG}}{V_L}\right) \quad (6)$$

Using the angle of transformation (θTR) in Fig. 2, the references rotor currents (i*ra, i*rb, and i*rc) are obtained from I*qr and I*dr. Reference currents and rotor currents (iri, irb, and irc) are used to create RSC gating signals with a PWM controller.

B. Control Algorithm for LSC

You can see the LSC control method in Figure 3. To accomplish the following, the LSC is directed.

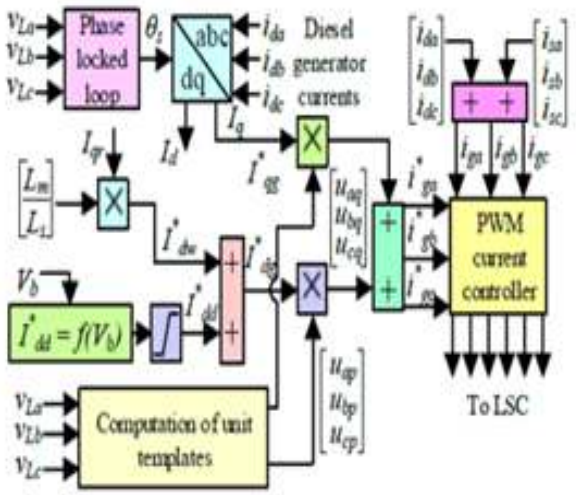

Figure 3. LSC control algorithm

It keeps the DFIG stator current sinusoidal and balanced. In order to maximize fuel economy, PDmin and PDmax denote the lowest and maximum DG power output, respectively. To make the standard currents as indicated in Fig. 3, a modified indirect control algorithm based on capacitance reference frame is utilized. To extract maximum output from of the DFIG and to manage the DG energy within the limit for optimum fuel usage, DG and DFIG stator vibrations are added and regulated. LSC's d-axis component is found to be equal to

$$I^{*}_{qr(k)} = I^{*}_{qr(k-1)} + K_{p\omega}\left(\omega_{err(k)} - \omega_{err(k-1)}\right) + K_{i\omega}\omega_{err(k)} \qquad (7)$$

Consider the equation: Idd, Idw = the type flow of DG and DFIG. Because Figure 3 illustrates that the saturating block is situated before the I*dd component, it can be concluded that the DG operates at its optimum fuel-efficient zone with a change in load, as shown. DG power is calculated depending on the states of the BES. To estimate the basic DG power (P*D) in Pumori, the calculation is done like this:

$$\omega_{err(k)} = \omega^{*}_{r(k)} - \omega_{r(k)} \qquad (8)$$

For these values of β, the value of beta ranges from 0 to 1. When BES is charged to its maximum voltage (Vbmax), then β is at its lowest value (Vbmin). In this particular instance, the V_T is from the form as

$$V_T = \sqrt{\frac{2}{3} \times \left(V_{pAG}^2 + V_{pBG}^2 + V_{pCG}^2\right)} \quad (9)$$

The constant parameters in (8) and (9) are represented by k1 and k2 respectively. k1 is chosen that which P*D attains its optimum fuel usage limit as β approaches one. To support this statement, note that k2 is used so that the β achieves unity at Vbmin. Appendices has the following values: PDmin, PDmax, Vbmax, Vbmin, k1, and k2.

the IID is calculated as,

$$I_{dc}^* = \left(\sqrt{2/3}\right) \times \left(\frac{P_D^* \times VA_{DG}}{V_L}\right) \quad (10)$$

The VL, which is equal to the base value for DG, and the VADG, which represents the V_T rating of DG, stand for the line voltage at PCC.

$$u_{Dp} = \frac{V_{pAB}}{V_T}, \quad u_{Dp} = \frac{V_{pBT}}{V_T}, \quad u_{Dp} = \frac{V_{pCB}}{V_T} \quad (11)$$

Idw= the equation Idw*= was calculated as

As illustrated in Fig. 3, the DG currents (ida, idb, and idc) are converted to Id and Iq by means of the angle of transformation (θs). Numerically, the q-axis element of LSC current (Iqg*) is equal to the q-axis component of DG current (Iq). According to Idg* and Iqg*, these current references are generated by multiplying an in-phase and a quadrature unit template with the Idg* and Iqg* in-phase and quadrature components, respectively, and then adding them together. Phase voltages (VA, VB, and VC) provide the unit templates as illustrated in Fig. 3. Component unit templates are produced as,

$$u_{ap} = \frac{v_a}{V_m}, u_{bp} = \frac{v_b}{V_m}, u_{cp} = \frac{v_c}{V_m} \quad (12)$$

Peak phase voltage is found at PCC, Vm being the result of the formula,

$$V_m = \{2(v_a^2 + v_b^2 + v_c^2)/3\}^{1/2} \quad (13)$$

in-phase components yields in-phase quadrature unit templates.

$$u_{aq} = -\frac{u_{bp}}{\sqrt{3}} + \frac{u_{cp}}{\sqrt{3}}, u_{bq} = -\frac{\sqrt{3}u_{ap}}{2} + \frac{u_{bp} - u_{cp}}{2\sqrt{3}}, \quad u_{cq} = -\frac{\sqrt{3}u_{ap}}{2} + \frac{u_{bp} - u_{cp}}{2\sqrt{3}} \quad (14)$$

Pulses produced by the LSC are applied to a PWM controller to create reference currents and sensing currents (iga, igb, and igc), as shown in Figure.

C. Solar PV array MPPT algorithm and Bidirectional Buck/Boost DC-DC converter Control

The bidirectional bucks or unidirectional boost DC-DC adapter is used to manage the DC link voltage by adjusting the flow of power from the BES. By doing so, the solar maximum power point is found. Here, a modified P & O method is utilized, which includes the steps of generating an estimated benchmark DC link voltage (V*dc) and then repeatedly sampling pulse generation (X). This illustration depicts the following procedures that are required to generate pulse 'X'. This is referred to as a sampling pulse in this instance.

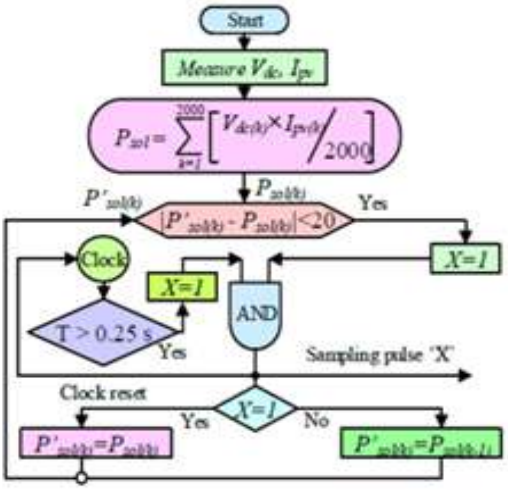

Figure 4. Sampling pulse generation

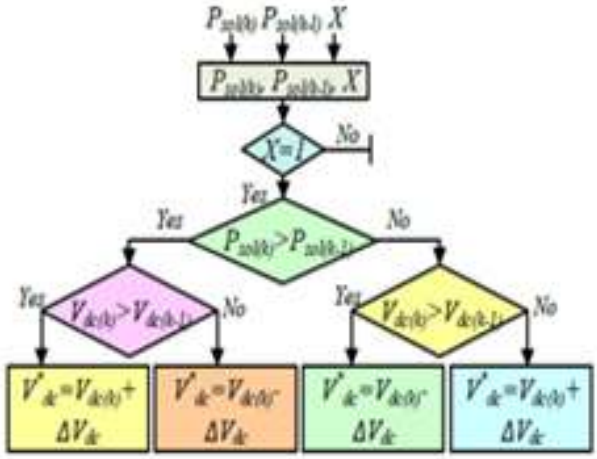

Figure 5. MPPT algorithm of solar PV array

Appropriate for variable ‘X'. The bit pattern changes between 0 and 1. For the circuit in Figure 4, you will need to gather the data for DC link voltage or solar PV voltage (Vdc) and solar PV current (Ipv) and calculate instantaneous solar power (also known as SPP). The second stage is the determination of Psol, which is the running average of solar power. When the running average power (Psol) is less than 20 W and a time delay of 0.25 s from the preceding sampling was not violated, the control is signifying that steady state has been reached. When the constant flow of information has been maintained, the output of the sampling pulse ‘X' becomes ‘1'. Incremental change in DC link voltage (V*dc) or solar PV MPPT voltage is triggered by the sampling pulse. V*dc is only updated if the sampling pulse is '1'. Figure 5 shows how the updated P&O MPPT algorithm behaves. If Psol(k) is greater than Psol, then the MPPT algorithm tests for psol(k)>psol (k-1). If the answer is affirmative, it will again test for the Vdc(k) being greater than Vdc (k-1). If the reference DC link voltage is also affirmative, then V*dc = Vdc(k)+ ΔVdc.

For every progressive progress in DC link voltage, there is a corresponding ΔVdc Scenarios different than this one are shown in Figure. Unidirectional buck/boost DC-DC converter control that is used in certain applications. This DC link voltage regulation is provided by the outside proportional-integral (PI) controller for the bilateral buck or bidirectional DC-DC boost converter management. Fig. 6 also shows the current output of the outer PI controller, which is standard battery current (I*b). The reference battery current is tracked using the inner PI controller. In addition, the duty ratio (R) of the unidirectional buck/boost DC-DC converter is produced by the inner PI controller. The standard bank current (I*b) is derived by dividing 6 by the battery's DC current.

$$I^{*}_{b(k)} = I^{*}_{b(k-1)} + K_{pb}(V_{dc(k)} - V_{dc(k-1)}) + K_{ib}V_{dc(k)} \quad (15)$$

Error occurs when the DC connection voltage drops at the kth instant. In the chart below, Vdc(k) and V*dc(k) are the voltage reference at reference time (kth) and the voltage measured at reference time (kth). proportional and Outer PI controller integral constants. By the way, the bidirectional DC-DC converter's duty ratio (R) is calculated as:

$$R_{(k)} = R_{(k-1)} + K_{pv}(I_{bo(k)} - I_{bo(k-1)}) + K_{v}I_{bo(k)} \quad (16)$$

Hence, the battery current current was incorrect at the kth moment is Here Ib(k) and Ib(k) refer to the current flowing in the reference battery at the kth moment. To transform the acquired duty ratio (R) into PWM signals, the duty ratio obtained is applied to the PWM generator.

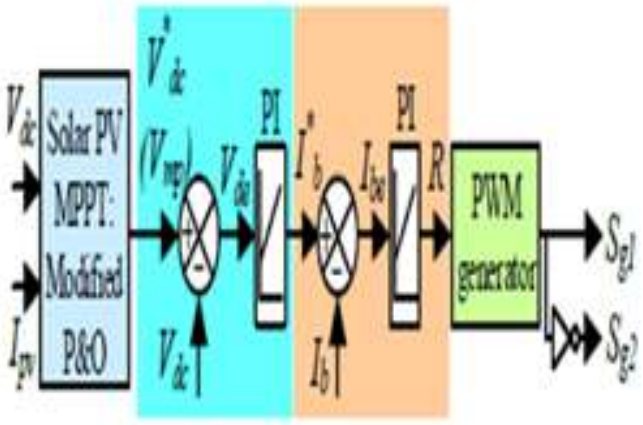

Figure 6. Control of bidirectional buck or bidirectional boost converter

III. DEVELOPING CONTROL FOR THE NEW SCHEME

Although having few disadvantages, PID controls are one of the major industrial control systems because of its benefits such as simple construction, excellent stability, good robustness, and easy modification. Nevertheless, it has a few shortcomings: the controller's settings cannot automatically change to accommodate a change in the external environment if the controlled object is moved. In conjunction with fuzzy logic, PI controllers are thought to be an appropriate solution for nonlinear and unpredictable processes. Conventional PI controllers are also coupled with FLCs in order to fine-tune their settings. An online updating of settings for a PI controller results in an improved performance for a fixed PI controller. This article proposes a combination of the benefits of an FLC with a standard PI controller, making use of a PI fuzzy control system structure.

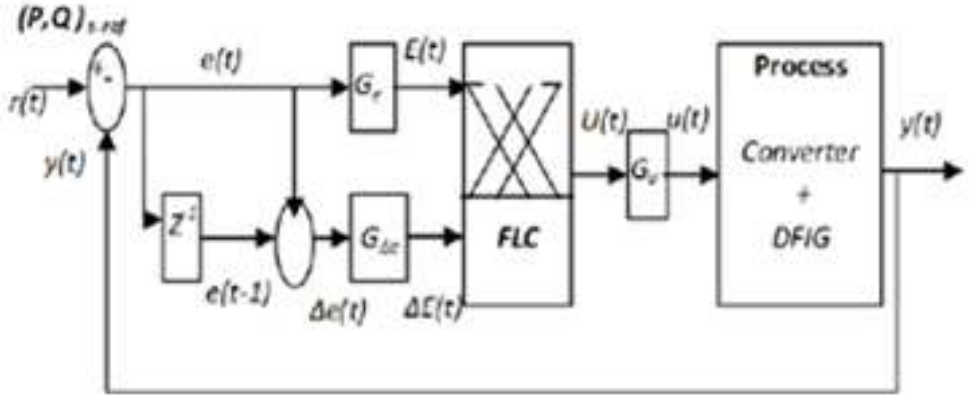

Figure 7. DFIG based microgrid with FLC controller

IV. RSC BASED SCHEME WITH THE FUZZY-PI HYBRID CONTROLLER

A. Analysis of Fuzzy Predictive Control

It has also been suggested that advanced mathematical prediction algorithms should be developed in order to predict variables that are required for the computation. Hybrid control schemes may be constructed by combining FLC with MPC to produce FPC. This theoretical examination of the suggested model is summarized below. Designs have been implemented in both MSC and FOC, including one for a PI controller to operate like a conventional control scheme. Traditional PI controllers cannot adjust for changes in KP and KI. Additionally, PI controlled systems are less sensitive to rapid changes in wind speed, which makes them more difficult to respond to in an emergency. As a consequence, the need of contemporary, durable controllers to comply with grid code and engineering guidelines increases. System control systems such as FLC are lately used in order to adjust system behavior and operations to match predefined specifications. For grid or load linked linear or non-linear loads, the FLC system may enhance the tracking performance as compared to conventional control systems. Fuzzy Predictive Control (FPC) is a hybrid control system that incorporates an FLC system controller with an MPC in order to achieve rapid responsiveness of the output signal. This FLC system utilized the schematic design of Figure 9 as a blueprint. Chapter 4 addressed the input and output variables that arise from the fundamental concepts. When dealing with a system's two input variables, the error e and the change in error Δe are important. The form of the membership functions of the rule base will influence the behavioural patterns of an FLC. This section focuses on the design of the FPC (flow control scheme) in relation to the FLC (flow control mechanism). Since this output is to be used as an input to MPC, it should be the reference value of iq. A collection of seven fuzzy subsets, named "Negative Big (NB), Negative Small (NS), Zero (Z), Positive Small (PS), and Positive Big" is used to give membership values to the linguistic variables (PB). In all instances, the input signal e is used for the signal of the FLC, while the output values of iq(k) are the values of the FLC (b). For the system's q circuit, e is the error between reference current signals $i*sd$ and $i*sq$ and the actual current signal. Likewise, for the d circuit, e is the error between the reference current signals $i*sd$ and $i*sq$ and the actual current signal. The interface engine, which comprises primarily of fuzzy rules and fuzzy implication sub blocks, receives fuzzified inputs and passes them on to the model.

Table 1 Rule base table of the Fuzzy controller

e \de	NB	NS	Z	PS	PB
NB	NB	NB	NS	NS	Z
NS	NB	NS	NS	Z	PS
Z	NS	NS	Z	PS	PS
PS	NS	Z	PS	PS	PB
PB	Z	PS	PS	PB	PB

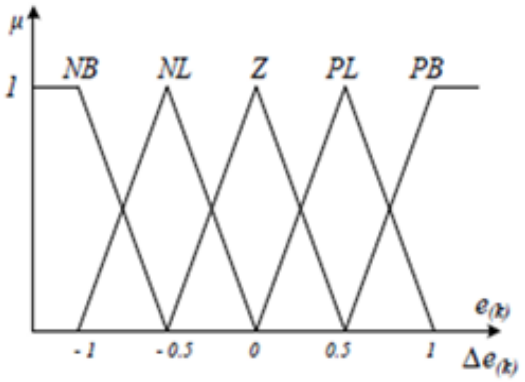

Figure 8. (a) Membership function of FLC for the input variables

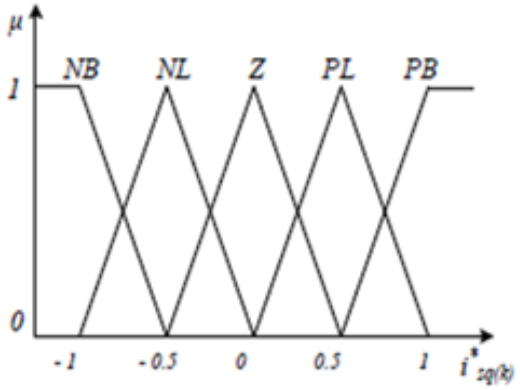

Figure 8. (b) Membership function of FLC for the output variables

To determine the output fuzzy set, the rule base is used to get an output fuzzy set. Once it is obtained, the fuzzy implication technique is used to identify the final output fuzzy set. Inferential techniques include techniques like the max-min inference approach. Table 1 illustrates the rules that govern the interface's fuzzy memory. Output fuzzy range is found if the fuzzification procedure is completed. The defuzzification procedure is required in this step in order to transform a fuzzy value of the control signal to a non-fuzzy one. This suggested approach makes use of the Centroid defuzzification technique, which reverses the defuzzification process.

B. Structure of the proposed technique

Designers will utilize FLC to build a diverse system in which neural networks, genetic algorithms, adaptive and predictive controls, and hybrid control systems are integrated to enhance output performance under unknown system parameters. The FPC system can regulate the generator and grid output currents simultaneously, which helps keep the system model under control. This algorithm, MSC, has been performed using controllers in this system.

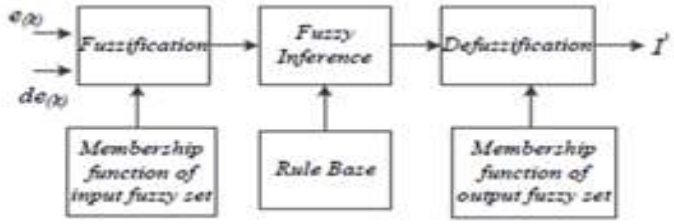

Figure 9. Structure of Fuzzy logic controller

V. SIMULATION RESULTS FOR THE NEW DFIG SCHEME

DFIG, DG, and solar PV array paired with BES is simulated in MATLAB to represent a microgrid utilizing wind turbine-driven DFIG, DG, and solar PV. Vr is the rms value of the phase voltage, fL is the system frequency, PD is the DG power, Pw is the wind power from the stator, Psol is the solar PV power, Vdc is the DC link voltage, Ib is the battery current, Vb is the battery voltage, Vw is the wind speed, G is insolation, Cp is the rotor power coefficient, PLa is the a-phase stator current, isa is the a-phase DG current, idab is the a-phase PCC voltage, LLa is the stator current, iLb and iLc are the load currents, iLn is the neutral current, and PLSC is the LSC current (icabc). The simulation's parameters are listed in Appendices.

A. Performance of Bidirectional Buck/boost DC-Dc converter at change in load

A two-way buck or boost DC-DC converter's performance is shown in Fig. 10. To get wind speed and insolation, the wind speed and insolation are both set to 7 m/s and 700 W/m2. The first load connected at PCC is a 3-phase balanced load of 2.5 kW. The DG is providing 4.84 kW, which is illustrated in Figure 10. Moreover, as can be shown in Fig. 10, the DFIG and solar PV array powers are 2.013 kW and 4.122 kW, respectively. As illustrated in Figure 10, this energy is sent to BES via a bidirectional buck/boost DC-DC converter. As time increases from 3 seconds to 5.5 seconds, a new load of 2 kW is attached and removed at regular intervals. It is noted that overall power production stays constant and additional load power is supplied by the BES via LSC during this time period. DC link voltage has a little sag and

swell, however the solar MPPT remains unaffected due to the shape of the Psol waveform. Finally, as shown in Figure 10, the network voltage and current are kept constant at all times.

B. System performance at variable wind speeds

The system's performance at varying wind speeds is seen in Figures 11 This configuration is linked to a 3-phase load of 4 kW, and the insolation is maintained at 700 W/m2. As can be shown in Fig. 11, the DG has a power output of 5.67 kW depending on the current condition of the BES. This plot illustrates the overall pattern of wind speed variation: Fig. 11. Fig. 11 depicts the controller regulating the DFIG rotor speed according to a wind-powered MPPT algorithm. The DC link voltage is also controlled. When DFIG speeds change from super-synchronous to sub-synchronous, the system dynamic reaction may be seen in Fig. 11. It has been found that the effect of wind MPPT varies in relation to the speed of the wind. Finally, the rotor current frequency, which governs the direction of the flow of DFIG, is altered to follow the RPM of the DFIG.

C. System performance at variable insolation

The system's performance varies with solar radiation, as shown in the figures. The wind speed remains constant at 7 m/s in this example. Additional, as shown in Fig. 12, the DG provides 4.2 kW of power using the battery voltage as the voltage reference. This setup connects a 3-phase, 3.9 kW linear balanced load at PCC. Fig. 12 shows the solar insolation variation between 700 W/m2 and 800 W/m2 from 3 s to 5.5 s. In order to meet the solar-level MPPT requirement, the DC link voltage is controlled by the bilateral DC-DC converter control, which is controlled by the two-way DC-DC converter controller. This is all represented by the Psol waveform in Figure.

D. System performance at unbalanced non linear load

Dynamic system performance, as shown in Fig. 13, is brought to an imbalanced nonlinear load. In the beginning, the grid at PCC has a 6.7 kW load balanced throughout both phases. Also, the nonlinear load is present, which causes the total load to be distributed over two phases. The circuit shown in Fig. 10 disconnects the load's a-phase at time 2.6 seconds, and then disconnects the load's phase-b at time 2.8 seconds. DFIG and DG voltages and currents follow the IEEE 519 standard. With the LSC, the linked load of PCC is in balance and produces more harmonic distortion and power output. Fig. 13 also depicts the LSC currents and neutral current. Furthermore, in Fig. 13, the power fluctuation in the unbalanced

nonlinear load is shown. Figure 13 illustrates several signal waveforms, including the voltages Vr, Vdc, Ib, Psol, Pw, PD, and PL. From these findings, it can be seen that the DC link voltage is controlled, and furthermore, it has been shown that DC link voltage regulation is without effect on solar PV and wind MPPT functioning. In regards to Ib, PL, and PLSC, the reduction in load power is headed towards BES via LSC, which is clearly shown in the Ib, PL, and PLSC waveforms. The price of VR (Virtual Reality) is kept at a fixed level.

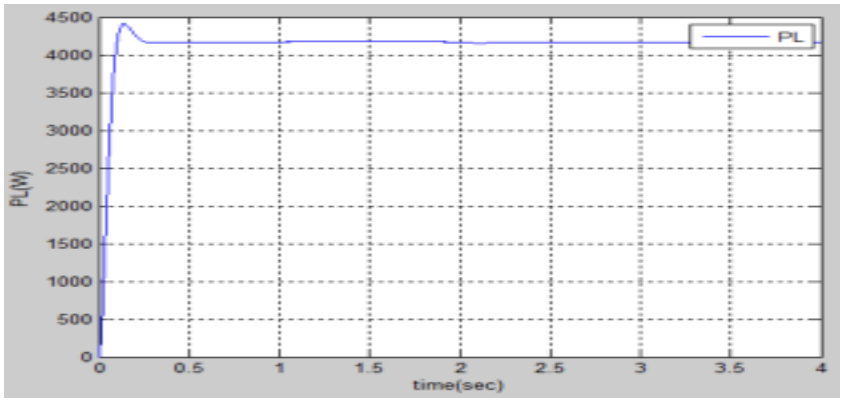

(a)

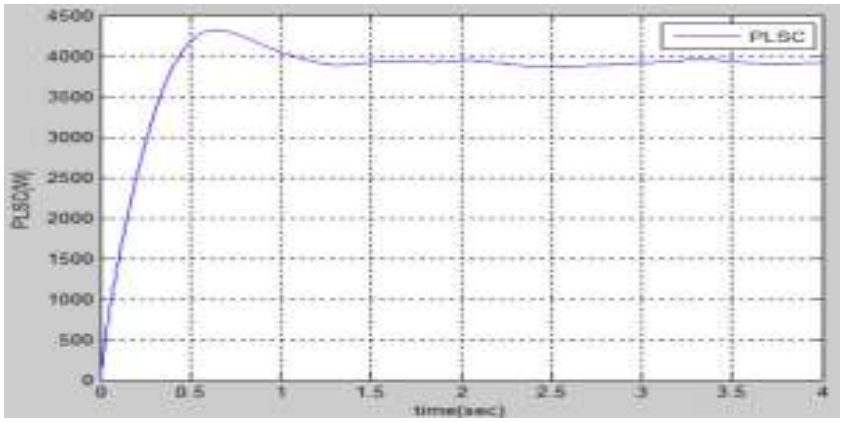

(b)

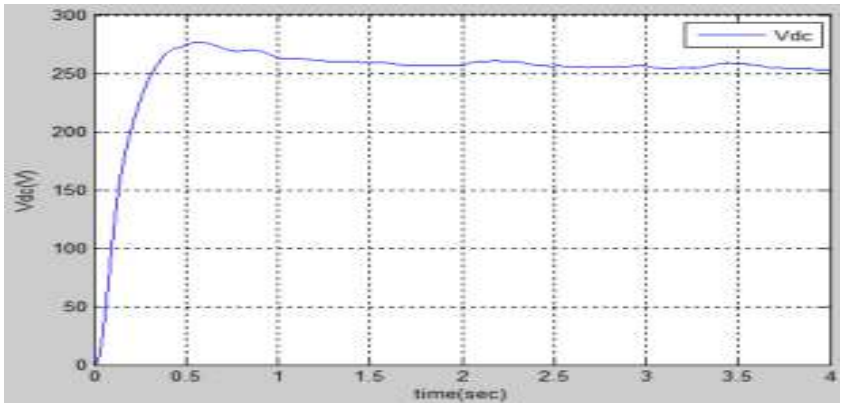

(c)

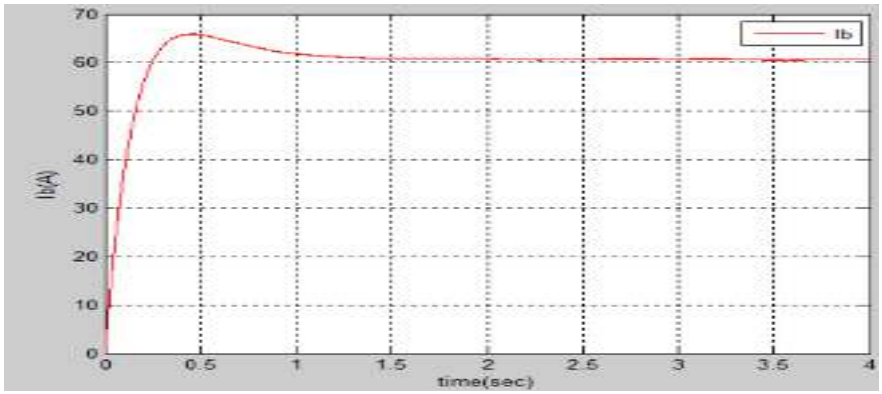

(d)

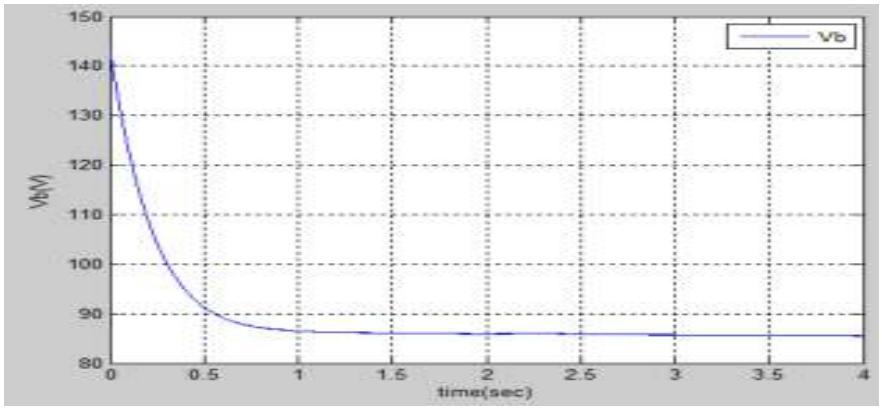

(e)

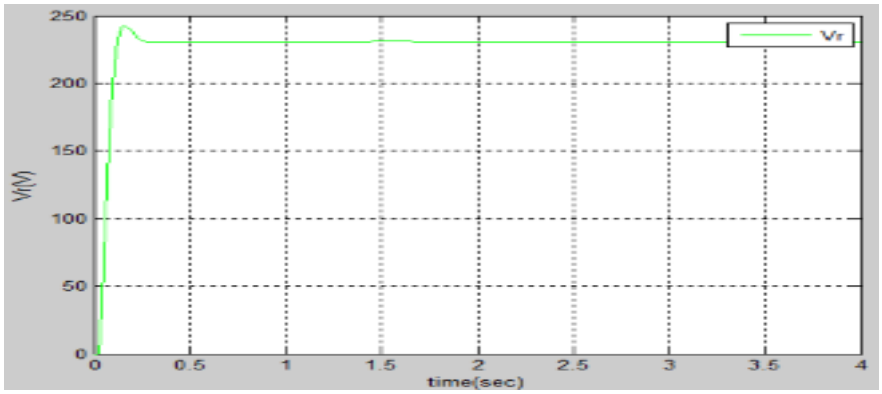

(f)

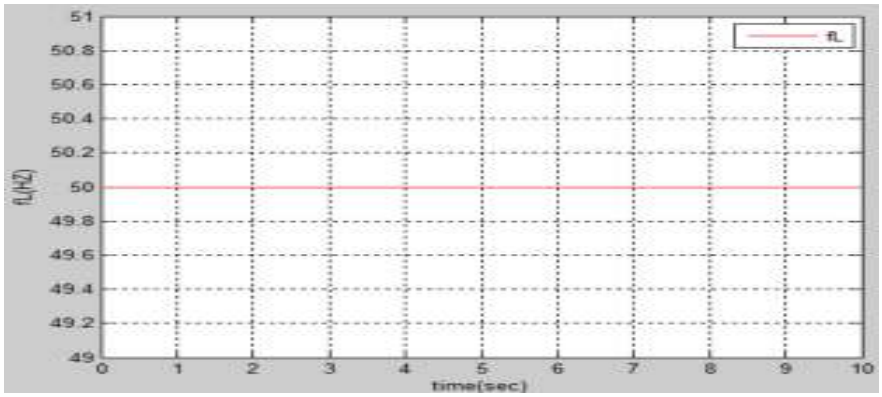

(g)

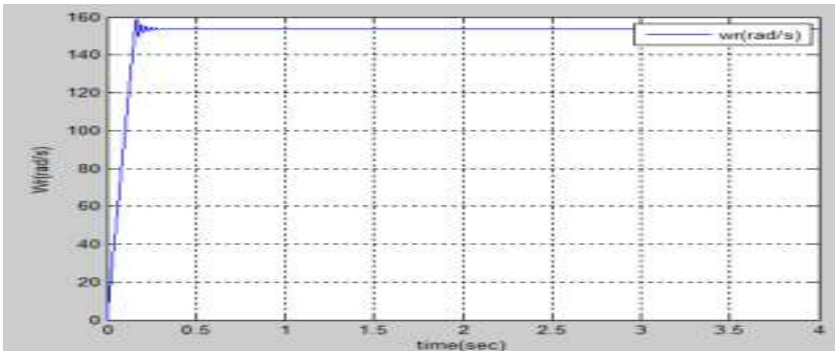

(h)

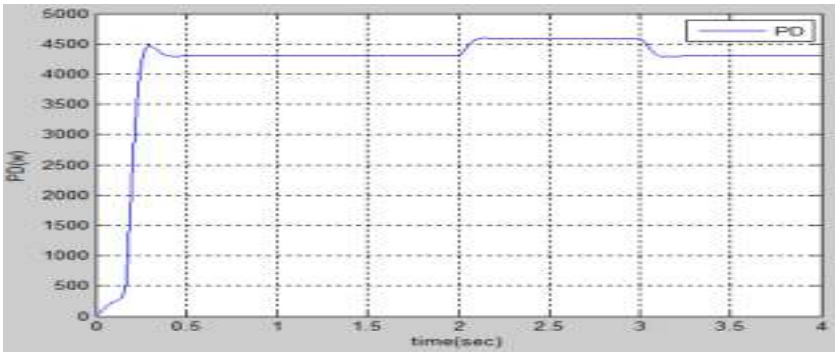

(i)

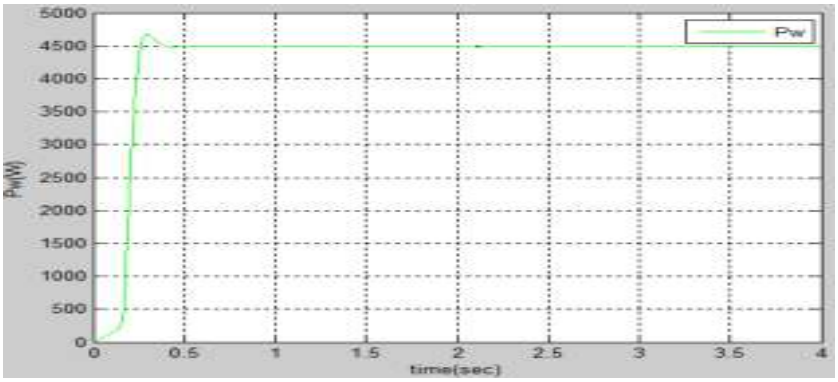

(j)

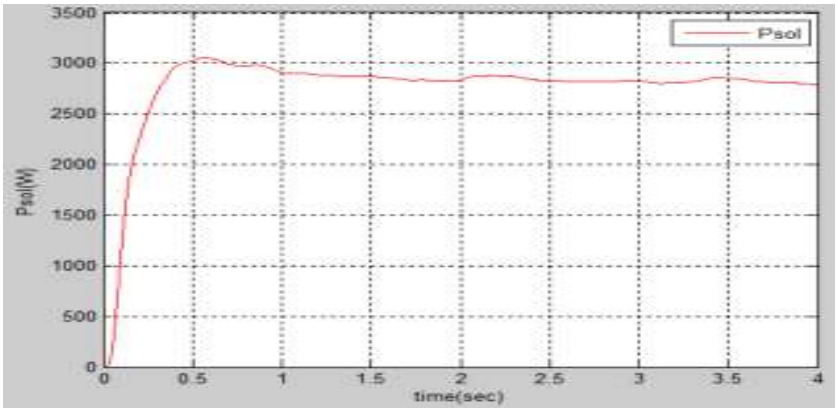

(k)

Figure 10. Performance of bidirectional buck/boost converter at change in load (a-k) PL, PLSC, V*dc*, I*b* and V*b*, V*r*, *fL*, *wr*, PD, P*w* and P*sol*

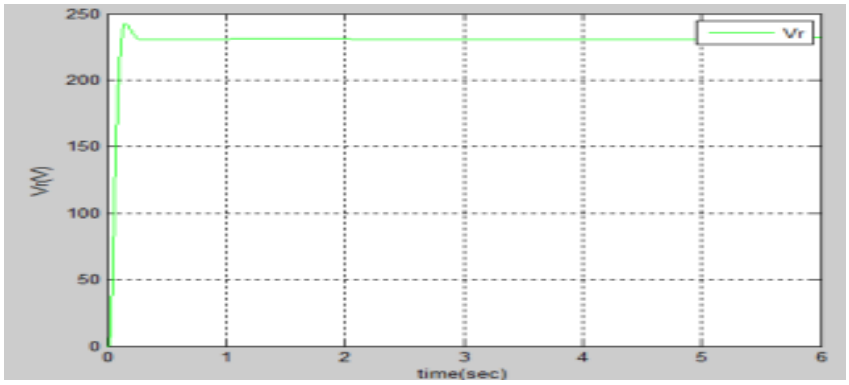
Vr
Vr(V)
time(sec)

(a)

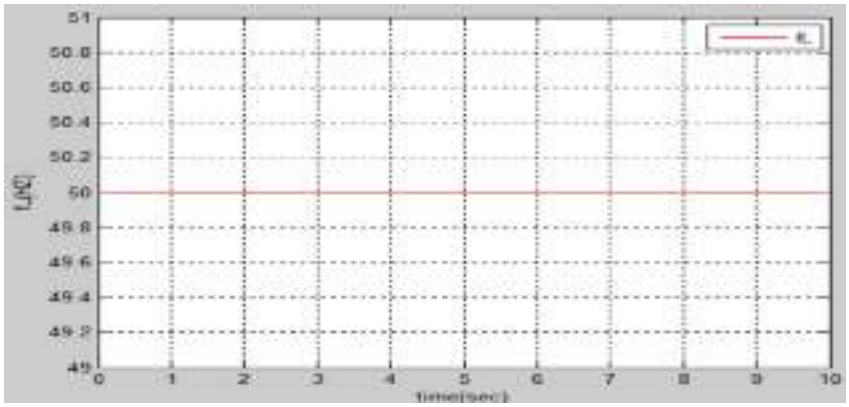
IL
IL(A)
time(sec)

(b)

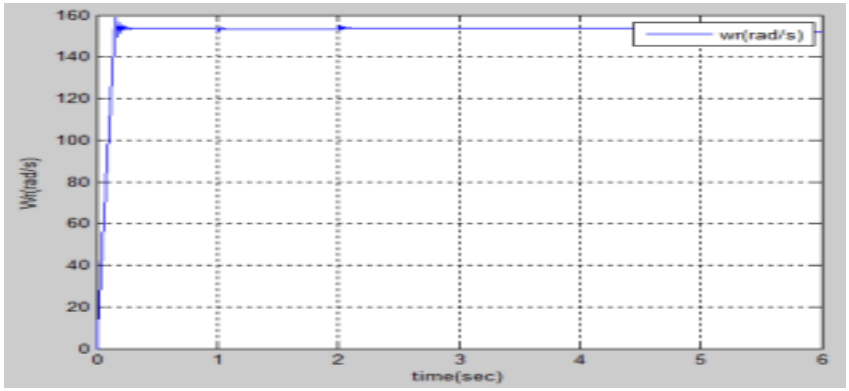
wr(rad/s)
Wr(rad/s)
time(sec)

(c)

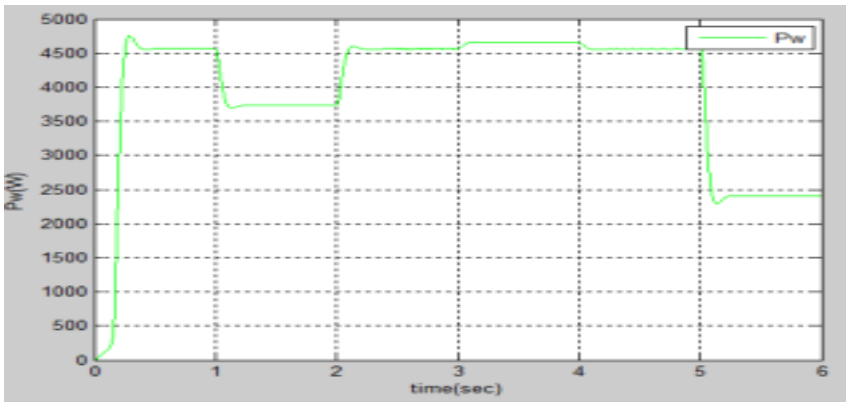
Pw
Pw(W)
time(sec)

(d)

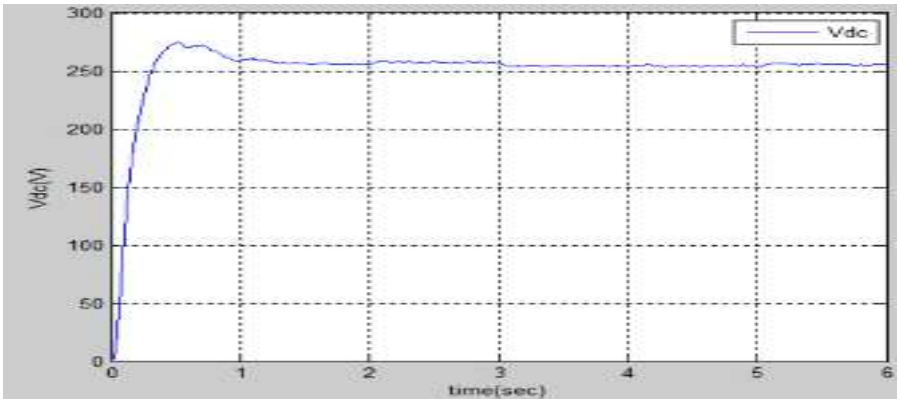
Vdc
Vdc(V)
time(sec)

(e)

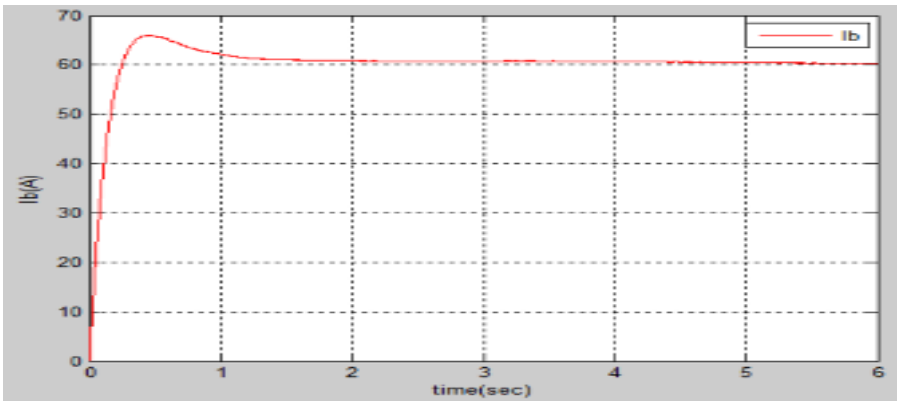
Ib
Ib(A)
time(sec)

(f)

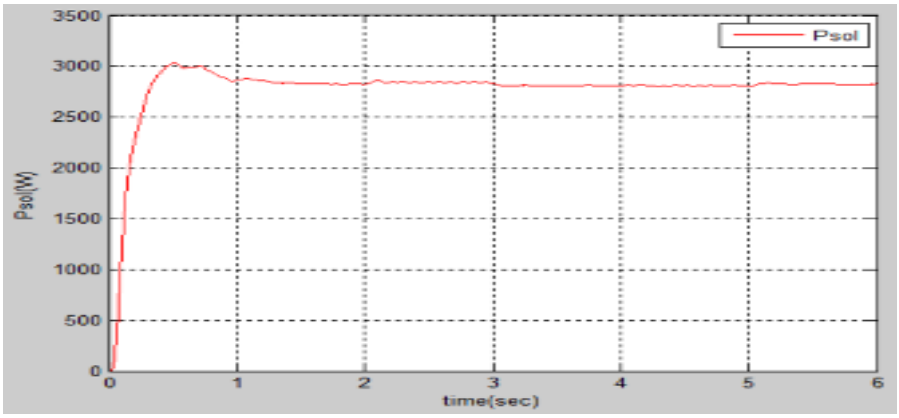
Psol
Psol(W)
time(sec)

(g)

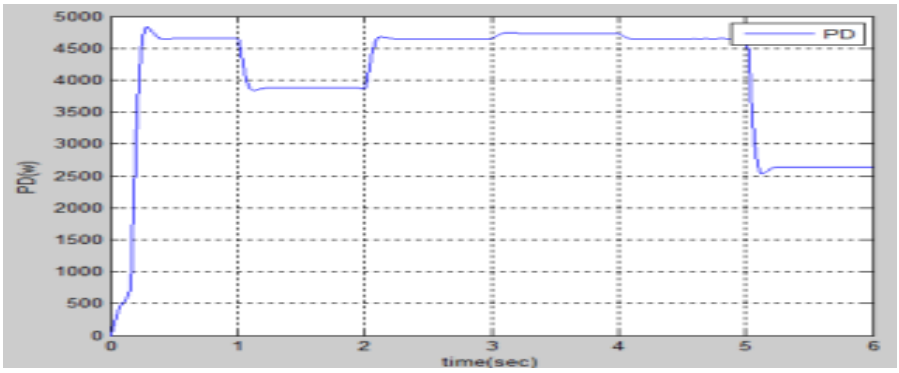
PD
PD(W)
time(sec)

(h)

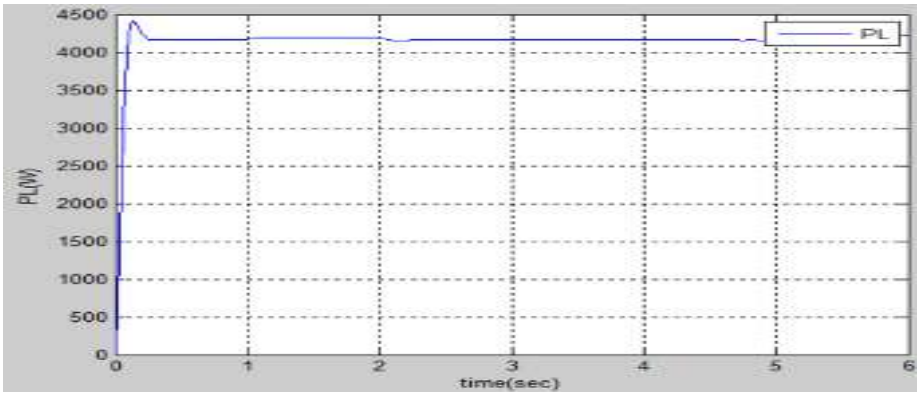
PL
PL(W)
time(sec)

(i)

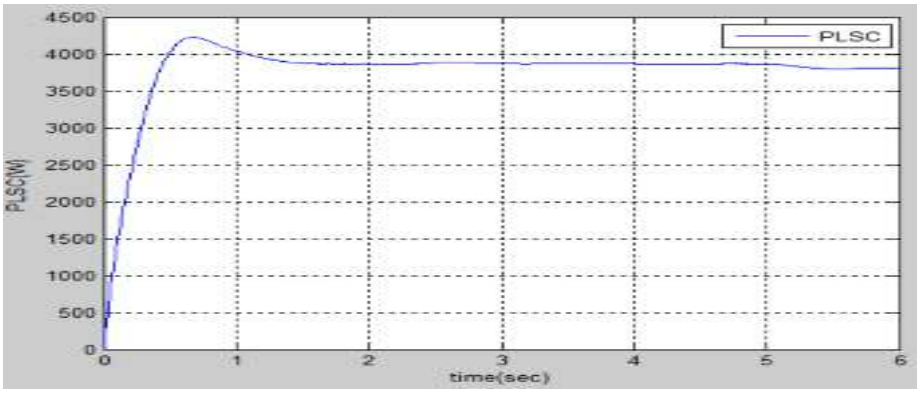
PLSC
PLSC(W)
time(sec)

(j)

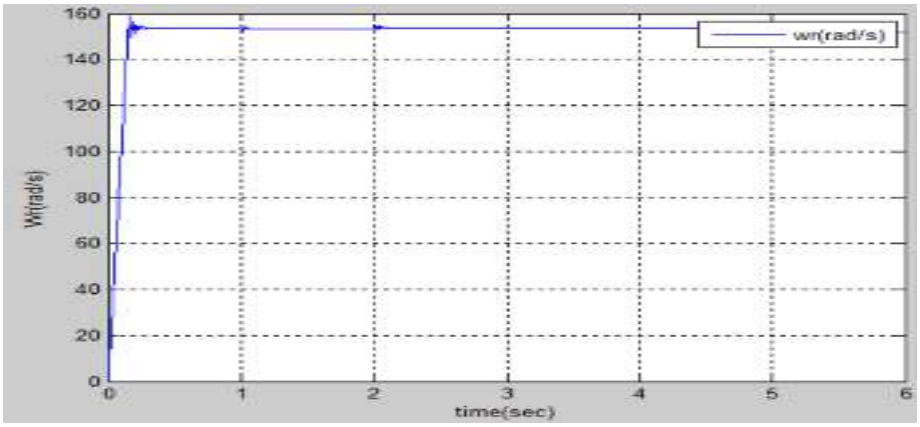
wr(rad/s)
Wr(rad/s)
time(sec)

(k)

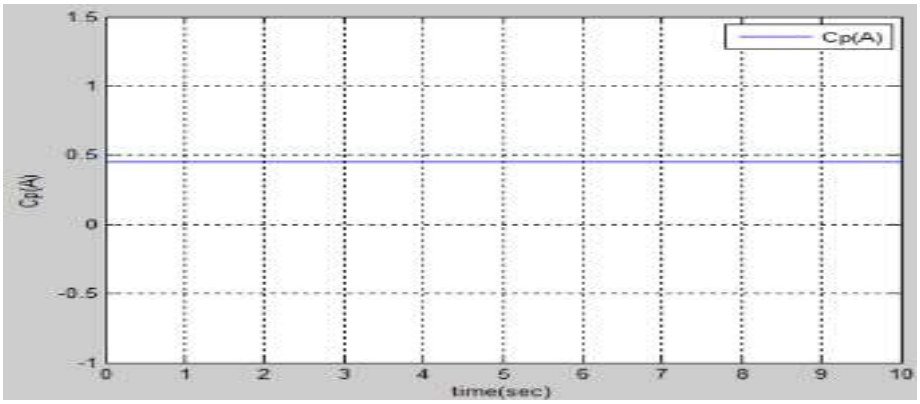
Cp(A)
Cp(A)
time(sec)

(l)

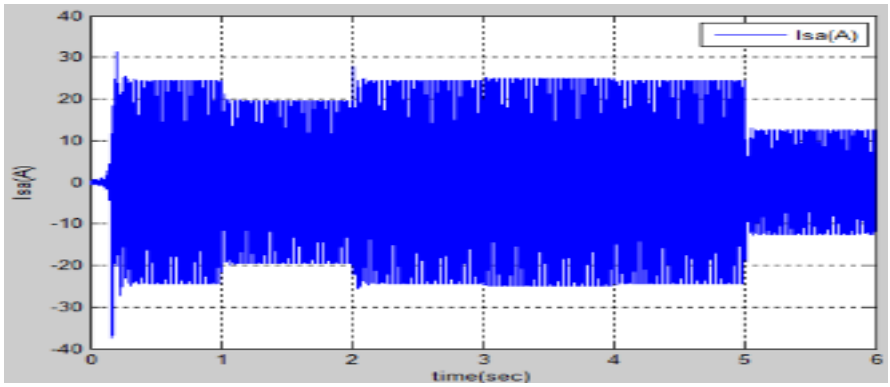

(m)

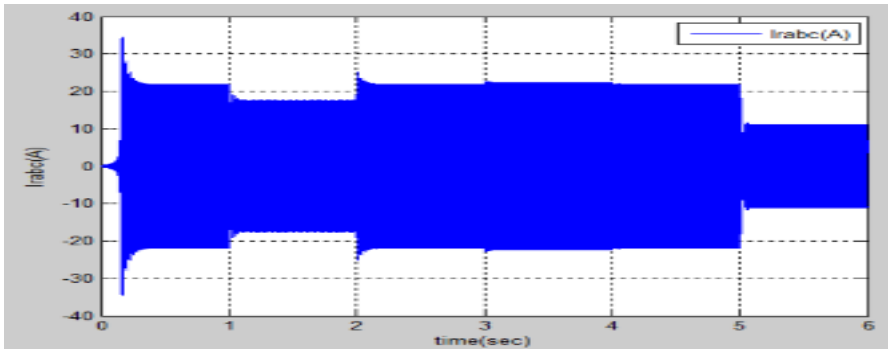

(n)

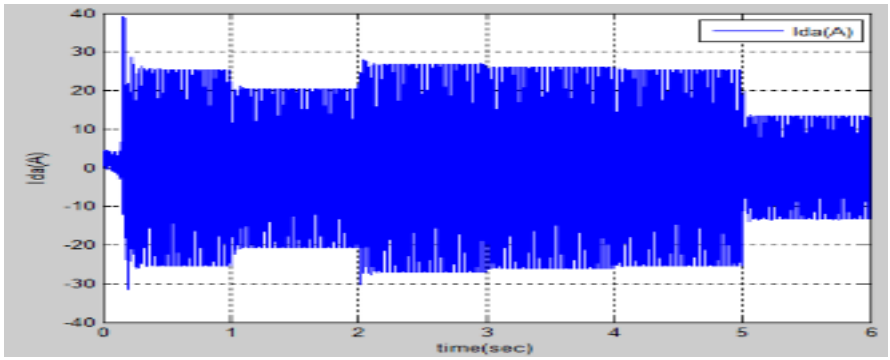

(o)

Figure 11. System performance at variable wind speed (a-j) V*r*, *fL*, V*w*, *wr* and P*w*, V*dc*, I*b*, P*sol*, PD, PL and PLSC, (k-o) system performance during changeover of DFIG speed from super synchronous to sub synchronous speed region: V*w*, *wr*, C*p*, *isa*, *irabc* and I*da*.

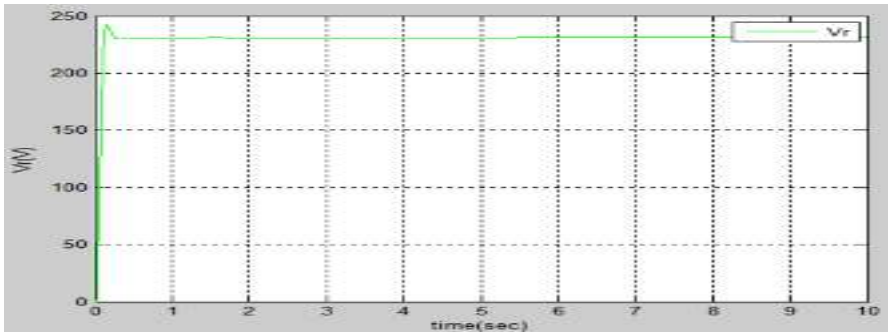

(a)

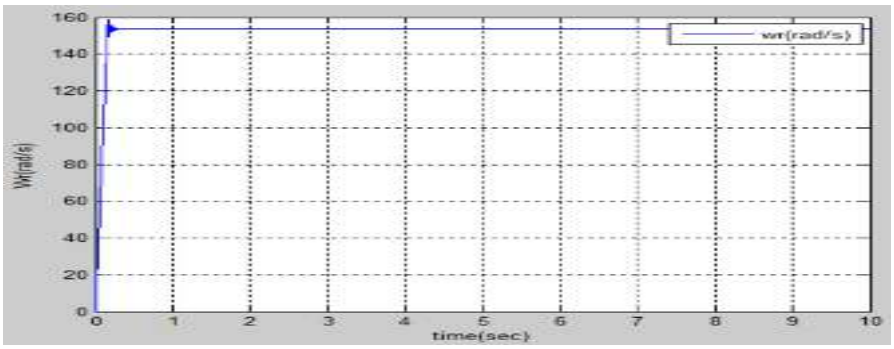
wr(rad/s)
Wr(rad/s)
time(sec)

(b)

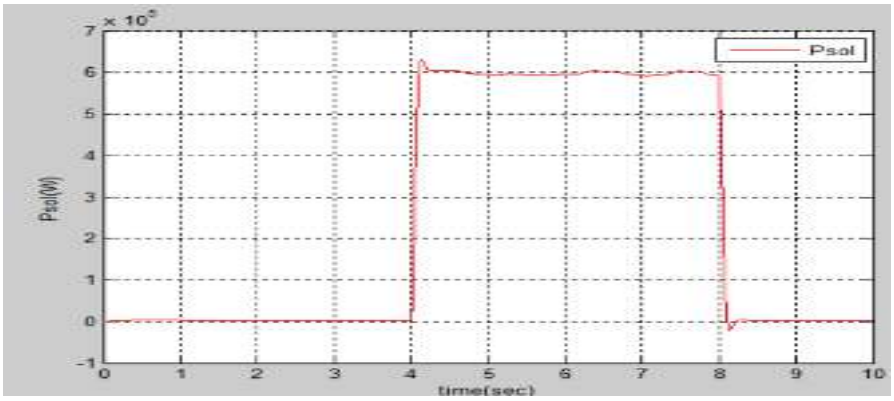
x 10^6
Psol
Psol(W)
time(sec)

(c)

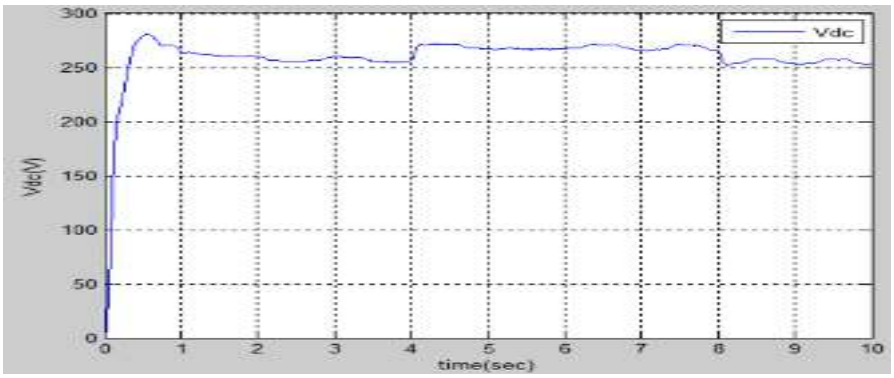
Vdc
Vdc(V)
time(sec)

(d)

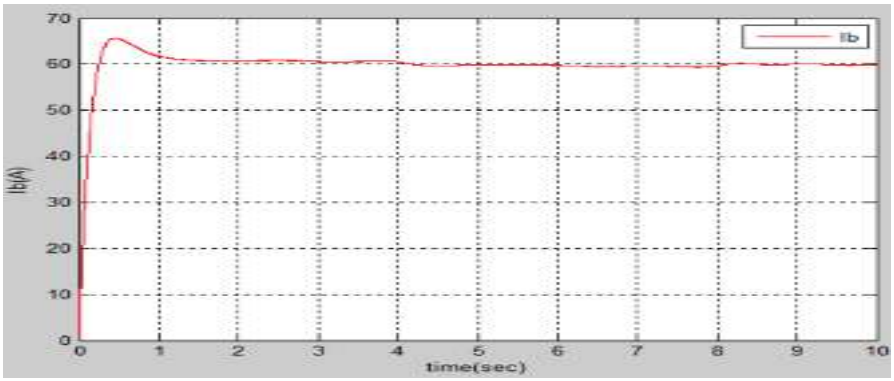
Ib
Ib(A)
time(sec)

(e)

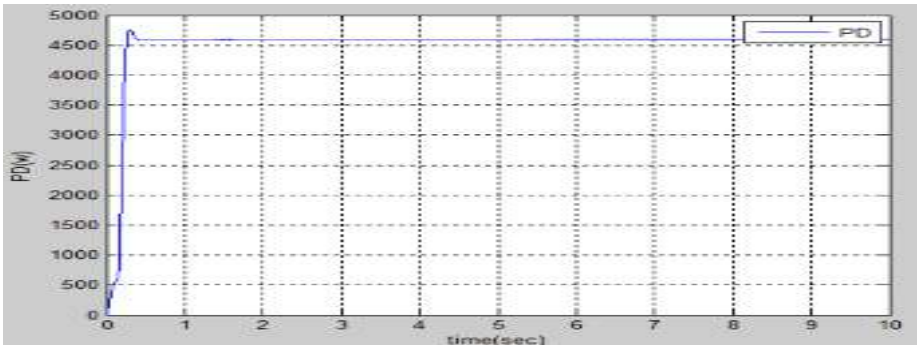

(f)

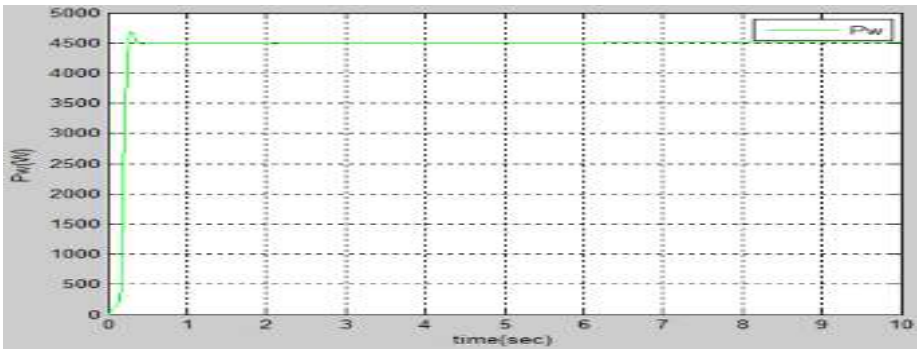

(g)

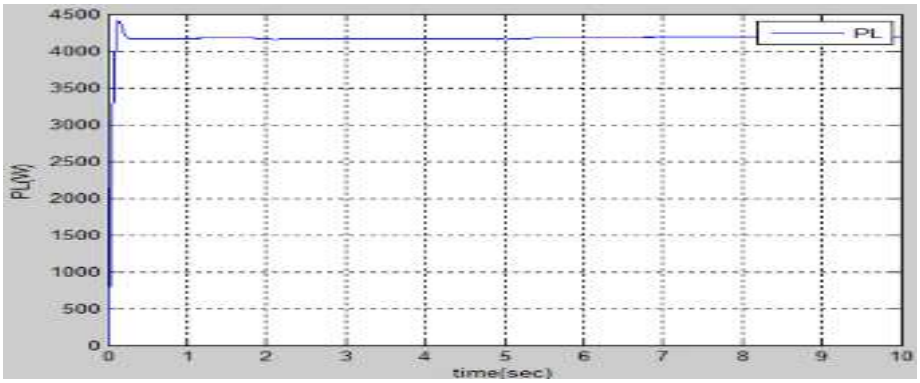

(h)

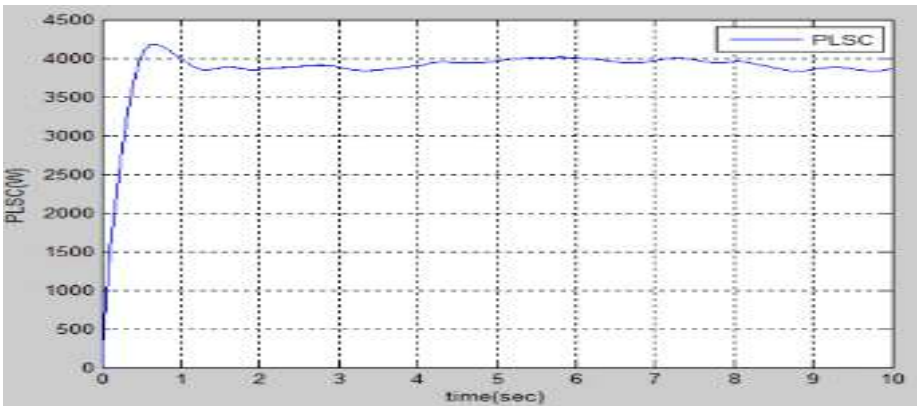

(i)

Figure 12. System performance at variable insolation (a-d) V*r*, *wr*, G, P*sol* and V*dc*: (e-i) I*b*, *PD, Pw, PL* and *PLSC*

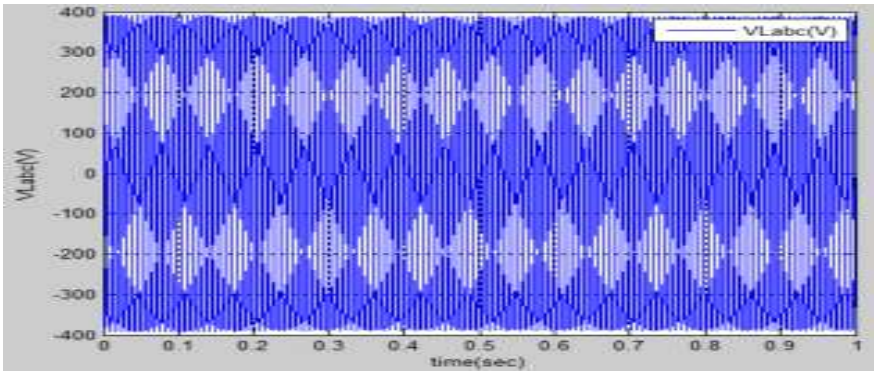
VLabc(V)
VLabc(V)
time(sec)

(a)

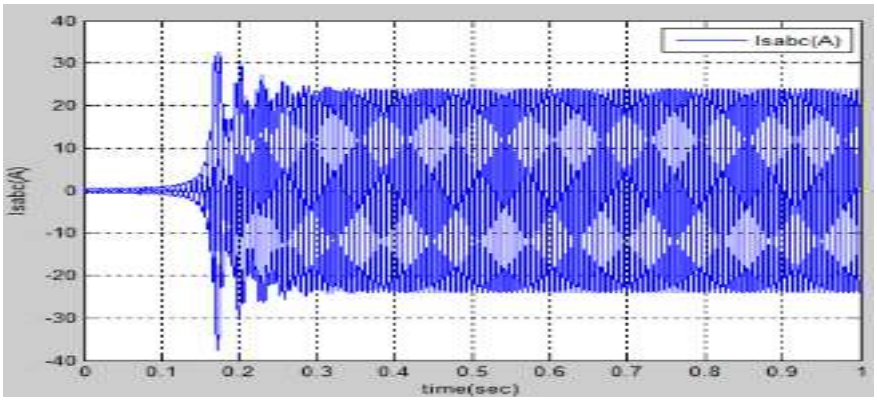
Isabc(A)
Isabc(A)
time(sec)

(b)

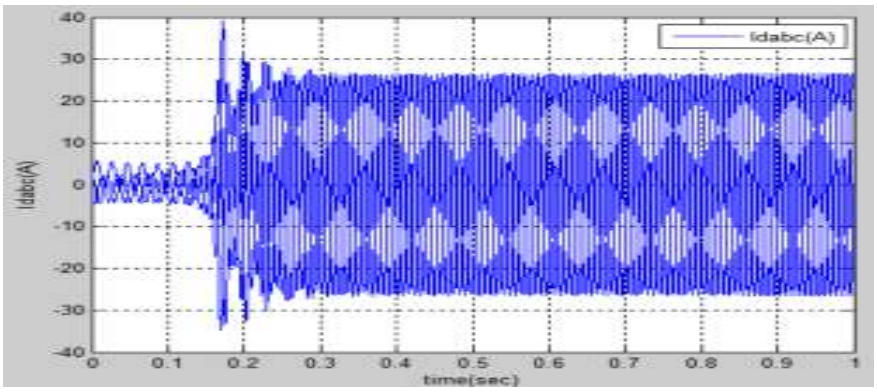
Idabc(A)
Idabc(A)
time(sec)

(c)

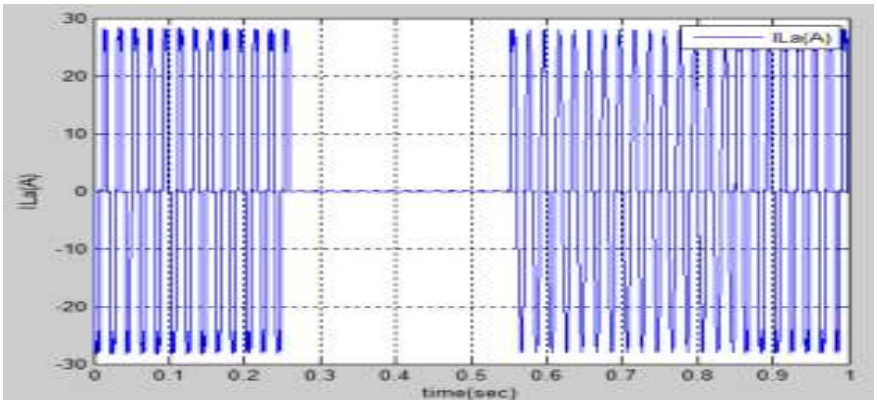
ILa(A)
ILa(A)
time(sec)

(d)

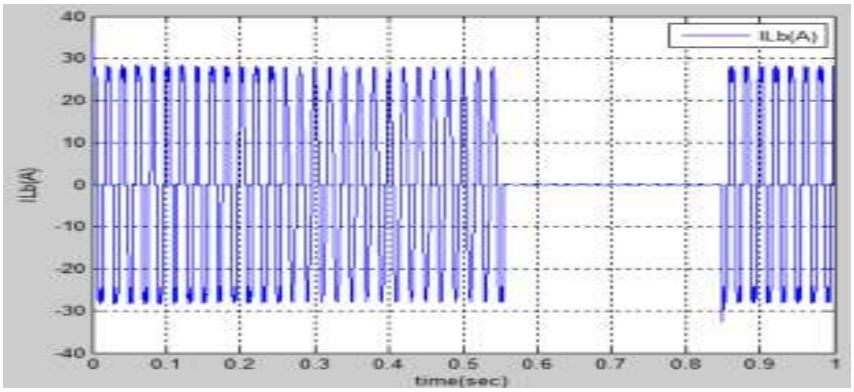
ILb(A)
ILb(A)
time(sec)

(e)

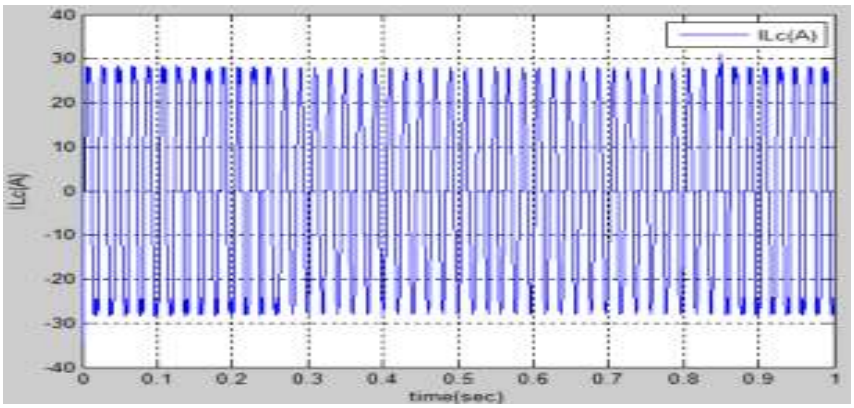
ILc(A)
ILc(A)
time(sec)

(f)

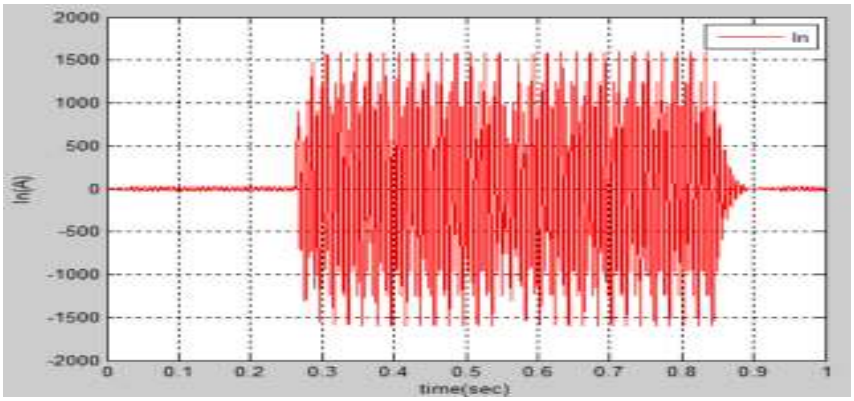
In
In(A)
time(sec)

(g)

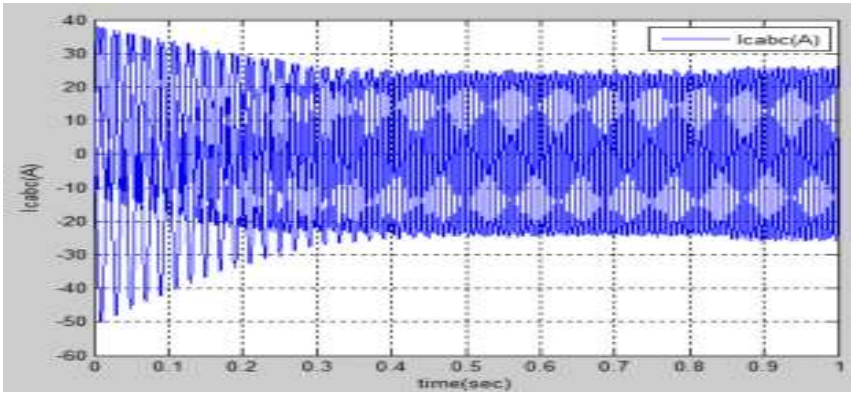
Icabc(A)
Icabc(A)
time(sec)

(h)

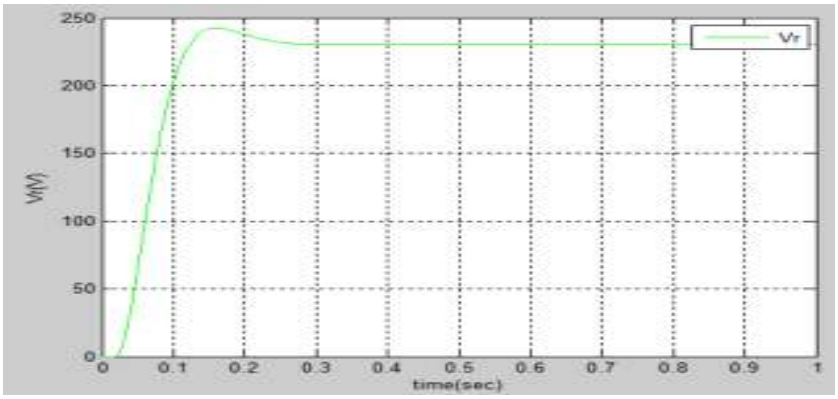
Vr
Vt(V)
time(sec)

(i)

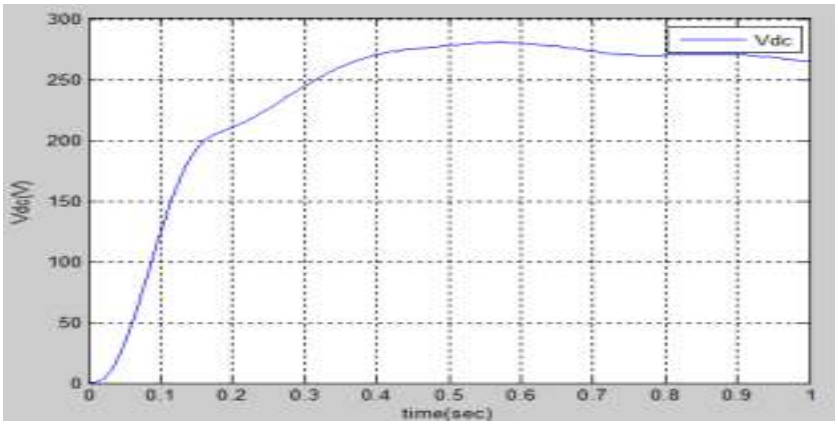
Vdc
Vdc(V)
time(sec)

(j)

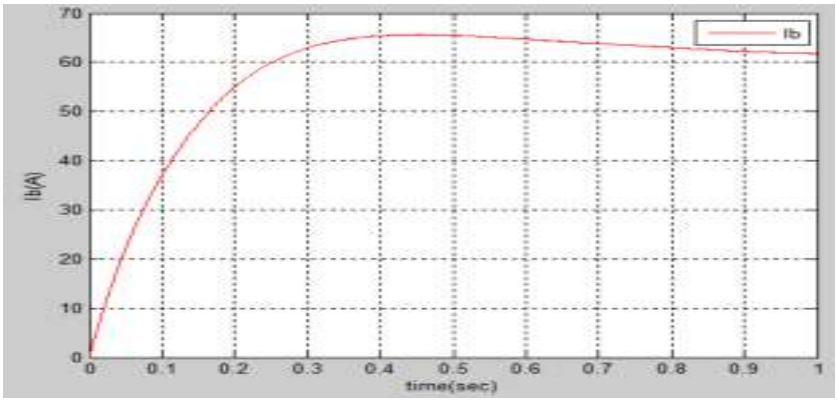
Ib
Ib(A)
time(sec)

(k)

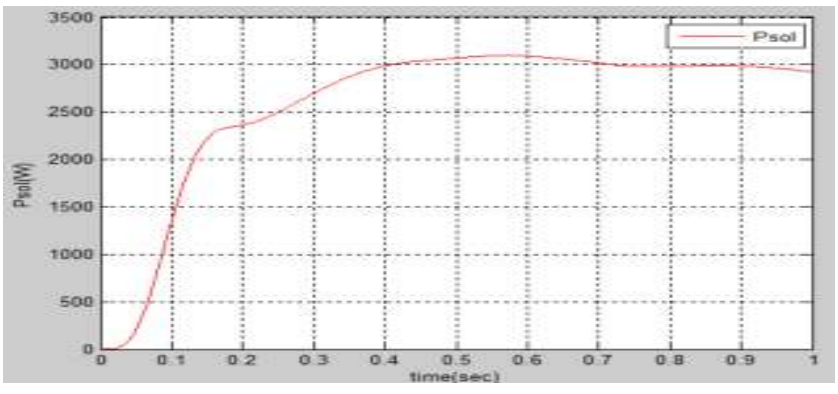
Psol
Psol(W)
time(sec)

(l)

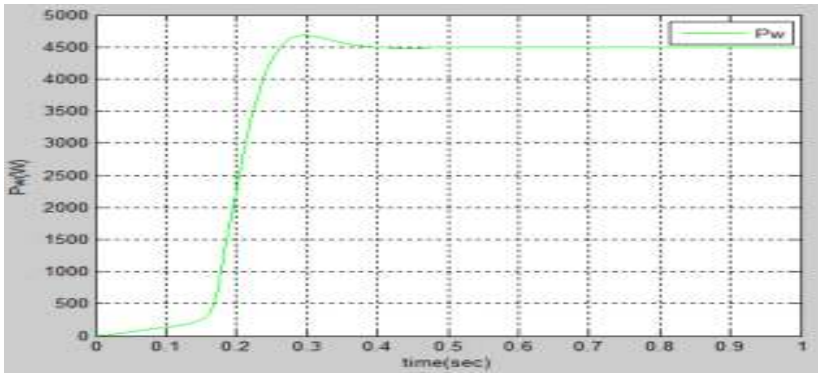

(m)

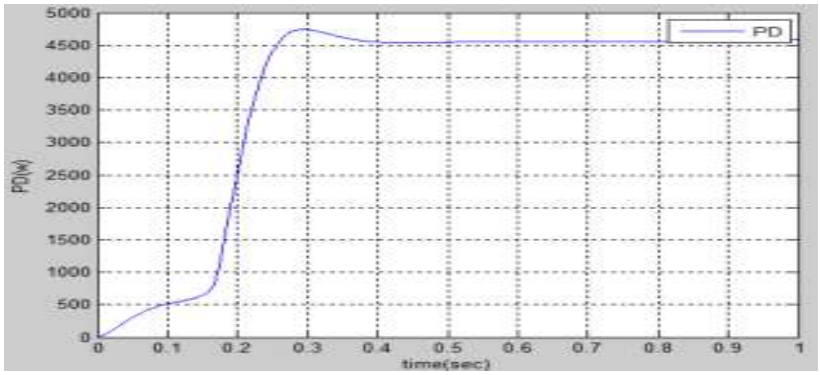

(n)

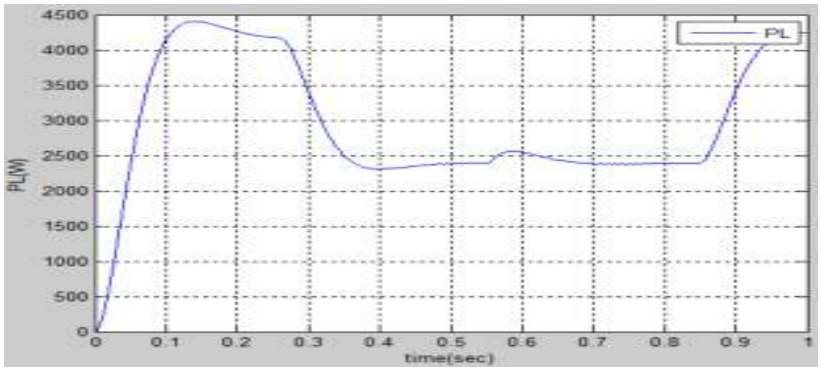

(m)

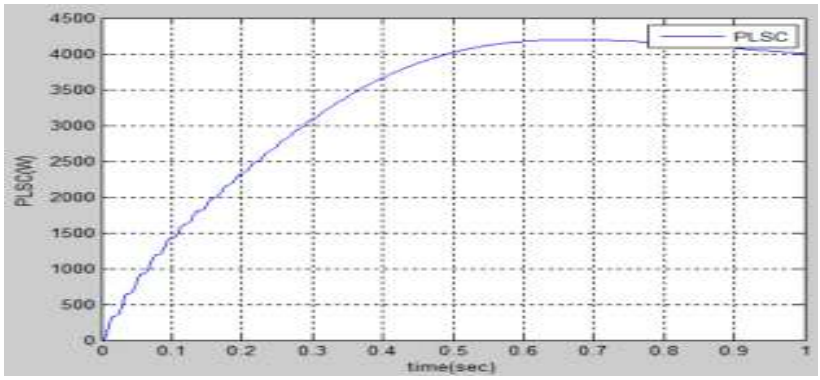

(o)

Figure 13. System performance at nonlinear unbalanced load: V*r*, V*dc*, I*b*, P*sol*, P*w*, *PD, PL* and *PLSC*

VI. CONCLUSİON

A new kind of adaptive PI control (Adap-conc-feed-Lc) with fuzzy logic is a DFIG that is powered by a wind turbine and is combined with an FLC-based control system. The DFIG PI controller optimization using the FUZZY-PI method is utilized in small signal slope stability to find the best parameter settings for the DFIG PI controllers. For a fast and accurate prediction, an FLC with a basic structure and adequate accuracy is developed, trained, and provided to users. DFIG transient performance is increased by the controllers, which alter PI gain levels depending on the various wind speeds. Using the suggested method, it was shown that the DFIG low frequency fluctuations could be successfully suppressed. The eigenvalue, damping ratio, and other indices indicate that DFIG has a much better transient performance and a similar improvement in long-term stability across a broad wind speed range.

REFERENCES

[1] J. Knudsen, J. D. Bendtsen, P. Andersen, K. K. Madsen, and C. H. Sterregaard, "Supervisory control implementation on diesel-driven generator sets," *IEEE Trans. Ind. Electron.*, vol. 65, no. 12, pp. 9698-9705, Dec. 2018.

[2] J. Jo, H. An, and H. Cha, "Stability improvement of current control by voltage feedforward considering a large synchronous inductance of a diesel generator," *IEEE Trans. Ind. Applicat.*, vol. 54, no. 5, pp. 5134-5142, Sept.-Oct. 2018.

[3] Y. Zhang, A. M. Melin, S. M. Djouadi, M. M. Olama and K. Tomsovic, "Provision for guaranteed inertial response in diesel-wind systems via model reference control," *IEEE Trans. Power Systems*, vol. 33, no. 6, pp. 6557-6568, Nov. 2018.

[4] N. Nguyen-Hong, H. Nguyen-Duc, and Y. Nakanishi, "Optimal sizing of energy storage devices in isolated wind-diesel systems considering load growth uncertainty," *IEEE Trans. Ind. Applicat.*, vol. 54, no. 3, pp. 1983-1991, May-June 2018.

[5] W. Li, P. Chao, X. Liang, J. Ma, D. Xu, and X. Jin, "A practical equivalent method for DFIG wind farms," *IEEE Trans. Sustain. Energy*, vol. 9, no. 2, pp. 610-620, April 2018.

[6] T. Adefarati, R. C. Bansal, and J. John Justo, "Techno-economic analysis of a PV–wind–battery–diesel standalone power system in a remote area," *The Journal of Engineering*, vol. 2017, no. 13, pp. 740-744, 2017.

[7] C. Wu and H. Nian, "Stator harmonic currents suppression for DFIG based on feed-forward regulator under distorted grid voltage," *IEEE Trans. Power Electron.*, vol. 33, no. 2, pp. 1211-1224, Feb. 2018.

[8] N. K. Swami Naidu and B. Singh, "Experimental implementation of doubly fed induction generator-based standalone wind energy conversion system," *IEEE Trans. Ind. Applicat.*, vol. 52, no. 4, pp. 3332-3339, July-Aug. 2016.

[9] D. Sun, X. Wang, H. Nian, and Z. Q. Zhu, "A sliding-mode direct power control strategy for DFIG under both balanced and unbalanced grid conditions using extended active power," *IEEE Trans. Power Electron*., vol. 33, no. 2, pp. 1313-1322, Feb. 2018.

[10] Ju Liu, Wei Yao, Jinyu Wen, Jiakun Fang, Lin Jiang, Haibo He, and Shijie Cheng, "Impact of power grid strength and PLL parameters on stability of grid-connected DFIG wind farm," *IEEE Trans. Sustain. Energy*, vol. 11, no. 1, pp. 545-557, Jan. 2020.

[11] A. Thakallapelli, S. Kamalasadan, K. M. Muttaqi, and M. T. Hagh, "A synchronization control technique for soft connection of doubly fed induction generator based wind turbines to the power grids," *IEEE Trans. Ind. Applicat.*, vol. 55, no. 5, pp. 5277-5288, Sept.-Oct. 2019.

[12] P. Shah, I. Hussain, and B. Singh, "Single-stage SECS interfaced with grid using ISOGI-FLL-based control algorithm," *IEEE Trans. Ind. Applicat.*, vol. 55, no. 1, pp. 701-711, Jan.-Feb. 2019.

[13] A. K. Singh, I. Hussain, and B. Singh, "Double-stage three-phase grid-integrated solar PV system with fast zero attracting normalized least mean fourth based adaptive control," *IEEE Trans. Ind. Electron.*, vol. 65 no. 5, pp. 3921-3931, May 2018.

[14] M. J. Morshed and A. Fekih, "A novel fault ride through scheme for hybrid wind/PV power generation systems," *IEEE Trans. Sustainable Energy*, Early Access.

[15] S. K. Tiwari, B. Singh, and P. K. Goel, "Design and control of autonomous wind–solar system with DFIG feeding 3-phase 4-wire loads," *IEEE Trans. Ind. Applicat.*, vol. 54, no. 2, pp. 1119-1127, March-April 2018.

[16] Y. Zhang, J. Wang, A. Berizzi, and X. Cao, "Life cycle planning of battery energy storage system in off-grid wind–solar–diesel microgrid," *IET Gener., Trans. & Distr.*, vol. 12, no. 20, pp. 4451-4461, Nov. 2018.

[17] S. K. Tiwari, B. Singh, and P. K. Goel, "Control of wind–diesel hybrid system with BESS for optimal operation," *IEEE Trans. Ind. Applicat.*, vol. 55, no. 2, pp. 1863-1872, March-April 2019.

[18] K. Venkatraman, B. Dastagiri Reddy, M. P. Selvan, S. Moorthi, N. Kumaresan, and N. A. Gounden, "Online condition monitoring and power management system for standalone

micro-grid using FPGAs," *IET Gener., Trans. & Distr.*, vol. 10, no. 15, pp. 3875-3884, Nov. 2016.

[19] S. Puchalapalli and B. Singh, "A single input variable FLC for DFIG-based WPGS in standalone mode," *IEEE Trans. Sustainable Energy*, vol. 11, no. 2, pp. 595-607, April 2020.

[20] J. Hussain and M. K. Mishra, "Adaptive maximum power point tracking control algorithm for wind energy conversion systems," *IEEE Trans. Energy Convers.*, vol. 31, no. 2, pp. 697-705, June 2016.

[21] S. Puchalapalli, S. K. Tiwari, B. Singh, and P. K. Goel, "A microgrid based on wind driven DFIG, DG and solar PV array for optimal fuel consumption," in *8th IEEE Power India International Conference (PIICON)*, Kurukshetra, India, 2018, pp. 1-6.

[22] Cheng, H., Zhang, D., Cheng, L. Comparative Study on Fuzzy PID Controller and Conventional PID Controller. Applied Mechanics and Materials, 328: 112-116. https://doi.org/10.4028/www.scientific.net/AMM.328.112